

Numerical simulation of two-phase droplets on a curved surface using Surface Evolver

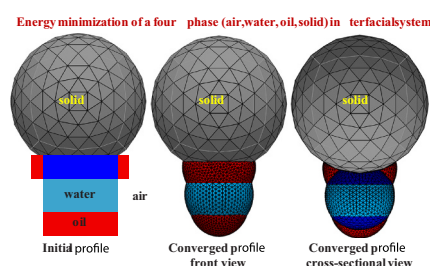
M. Jamali, H. Vahedi Tafreshi^{1,*}

Department of Mechanical and Aerospace Engineering, North Carolina State University, Raleigh, North Carolina 27695-7910, United States

HIGHLIGHTS

- Droplet shape on a curved surface is simulated in a magnetic field using Surface Evolver.
- The use of solid–liquid surface energy is proposed for Surface Evolver simulations.
- Effective surface tension can be used in Surface Evolver to simulate a two-phase droplet.
- Modeling of multiphase droplets is feasible using the proposed solid–liquid energy approach.

GRAPHICAL ABSTRACT



ARTICLE INFO

Keywords:

Compound droplet
Surface evolver
Multiphase droplet
Ferrofluid droplet
Interfacial phenomena

ABSTRACT

In this paper, we present a new approach for using the Surface Evolver (SE) finite element program to simulate the 3-D shape of a droplet on a curved surface. The approach proposed in this paper circumvents the need for carrying out complicated derivations to obtain analytical expressions for the total energy of the interfacial areas between air, liquid, and solid surfaces. More specifically, we use the solid–liquid surface energy in place of the contact angle when simulating a droplet using SE. This approach also makes it easier to use SE to model a two-phase droplet (e.g., a compound droplet) on a solid surface. To better illustrate our approach, the 3-D shape of single-phase and compound pendant droplets are simulated on a hydrophobic spherical surface in the presence of gravitational and magnetic fields. For validation purposes, our computational results are compared to dedicated experimental data obtained by compounding water droplets with oil-based ferrofluids of different surface tensions.

1. Introduction

The ability to predict the 3-D shape of a droplet on surfaces of different morphologies and to formulate the force required to detach the droplet from those surfaces is a complex interfacial problem of industrial importance. For instance, a surface can be made hydrophobic (or oleophobic) to prevent droplet spreading, but that does not necessarily

provide droplet mobility on the surface [1–3]. Quantifying droplet–surface interactions is important for a variety of applications including digital microfluidics [4–6], anti-icing [7,8], and self-cleaning applications in general [9–11]. This problem becomes even more complicated when the droplet is made of more than one liquid, e.g., a multiphase droplet on a dry surface or a single-phase droplet on a lubricant-infused surface [12–20]. Other engineering applications

* Corresponding author.

E-mail address: hvtafres@ncsu.edu (H.V. Tafreshi).

¹ URL: <http://mae.ncsu.edu/pmmf/>

benefiting from a deeper understanding of droplet–surface interactions include droplet filtration/separation (for the removal of dispersed droplets from a gas or liquid) [21–30], water management in fuel cells [31,32], fog harvesting [33,34], or drag reduction [35,36].

The ability to simulate the equilibrium shape of a two-phase droplet on a surface (a four-phase interfacial problem) allows us to answer various fundamental questions about how the droplet responds to external forces in terms of the volume and physical properties of its constituting fluids as well as the shape and physical properties of the solid surface. Conventional computational fluid dynamics (CFD) methods, such as volume of fluid (VOF) [37–40], level-set [41,42], or Lattice Boltzmann (LB) [43–46], can be used for such simulations. These methods however, require the entire volume of the simulation domain (the droplet and its surrounding volume) be meshed and therefore be included in the calculations (requiring excessive computational resources). This makes Surface Evolver (SE) an attractive option for conducting a numerical simulation to obtain the 3-D shape of a droplet on a surface. SE is a finite element code that uses an iterative method to obtain the equilibrium shape of the interface between two immiscible fluids (e.g., air and water) through minimizing the total energy of the system [47]. It is accurate with regard to enforcing the boundary conditions and it is quite efficient computationally as it only simulates the shape of the interfacial area between the phases in contact [47,48]. However, SE can only simulate equilibrium conditions (i.e., it cannot simulate the time-dependent dynamics of the detachment process or the effects of fluid viscosity) and one should consider a quasi-static approach to simulate droplet detachment using SE [49–54]. It is worth mentioning that one can also use a geometric approach, such as the cubic spline based method of [55,56], to obtain the shape of an axisymmetric droplet (or fluid–fluid interface).

This paper aims at introducing a new method for simulating a complex interfacial problem using the SE program. More specifically, the paper presents a simple but creative way of defining the total energy of a multiphase system in SE, and demonstrates the implementation of this method by simulating the detachment of a compound droplet from a spherical bead. The information presented in this paper can, for instance, be used to simulate the shape of a droplet on a lubricant-infused surface [12–20]. In the remainder of the paper, we first present a detailed discussion about simulating the equilibrium shape of a droplet on a curved surface using SE, which requires producing mathematical expressions for calculating the total energy of the system (i.e. the droplet on a curved surface) (Section 2.1). Later in Section 2.2, we present a new approach that not only allows one to circumvent the above-mentioned derivations, but also extend the application of SE program to the case of two-phase droplet simulations (four-phase interfacial problems) on different surface with different morphologies. These modeling strategies are referred to here as Method 1 and Method 2. As will be seen later in this paper, we explore ways to define an “effective surface tension” and an “effective contact angle” for a two-phase droplet such that they can be used to predict the force needed to detach the droplet from a surface (Section 3).

2. Simulating a single-phase droplet on a curved surface

In this section, we present the steps that are required to simulate the 3-D shape of a single-phase droplet on a curved surface using SE. We divide this section into two subsections. In the first subsection, we discuss the conventional method of simulating a droplet in which droplet contact angle with solid and droplet surface tension (i.e., air–water surface tension) are used as input (referred to here as Method 1). In the second subsection, we present our new approach where a less commonly-used quantity, the solid–water interfacial tension, is used as input in place of contact angle (referred to here as Method 2). As will be explained later in this paper, the second approach drastically simplifies the mathematical steps required to simulate a droplet using SE and allow the code to be used for multiphase droplet simulations. To simplify the

problem at hand, we have considered a spherical surface with a diameter comparable to that of the droplet in this section. This allows us to take advantage of the axial symmetry of the system when deriving mathematical equations or conducting complementary experiments. Obviously, such numerical simulations can be extended to the case of droplets on a flat surface by simply increasing the radius of curvature of the spherical surface.

2.1. Method 1

As mentioned earlier, SE obtains the 3-D shape of the interface between two immiscible phases through minimizing the total energy of the entire system considered in the simulation domain. Therefore, the first step is to define the total energy of the system correctly. Consider the case of a pendant droplet on a spherical bead as shown in Fig. 1. The system is a 5-faced cubic droplet with the edges of the 6th face (the missing face) representing the contact area with the bead. The missing 6th face can also be viewed as the droplet wetted area or the solid–liquid area. The blue, gray, and red colors represent the water droplet, bead, and droplet contact line (i.e., the edges of the 6th face). Note that, the bead itself is not a part of the system, and it is shown here for illustration only. In addition, the 5-faced cubic droplet shown in Fig. 1 is only an initial shape and its dimensions and location on the bead are arbitrary, but reasonable, values. Assuming that the water droplet maintains a Young–Laplace Contact Angle (YLCA) of θ_w^{YL} with the bead and that the

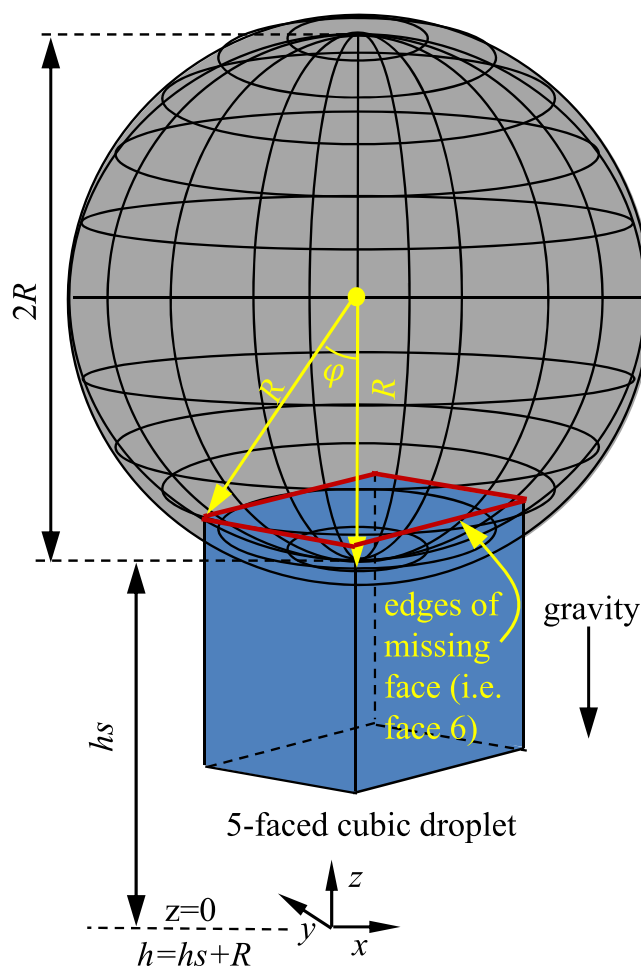


Fig. 1. A 5-faced cubic droplet on a solid sphere. The 6th face is excluded but represented with its edges on the sphere (i.e., contact line). Colors blue, gray, and red represent droplet, sphere, and the contact line, respectively. (For interpretation of the references to colour in this figure legend, the reader is referred to the web version of this article.)

droplet is under an arbitrary body force per unit mass (acceleration) of $f(z)$, the total energy of the system can be written as,

$$E_t = \sigma_{a-w}A_{a-w} - \sigma_{a-w} \cos \theta_w \iint_{A_{s-w}} dA + \iiint_w \rho_w U_{f(z)} dV \quad (1)$$

where σ , ρ , A , V are interfacial tension, droplet density, interfacial area, and droplet volume, respectively. Subscripts w , $a-w$, and $s-w$ represent water, air–water, and solid–water, respectively. $U_{f(z)}$ is a potential function for the acceleration function $f(z)$. In the absence of any additional external body force, $f(z)$ is assumed by default to be the gravitational acceleration g . To simulate the shape of a droplet using SE, one needs to input σ_{a-w} , θ_w^{YL} , and $U_{f(z)}$. The air–water interfacial area A_{a-w} will automatically be calculated by SE using the geometry of the aforementioned 5-faced cubic droplet. Note that, the solid–water interfacial area A_{s-w} (the missing 6th face of the cubic droplet) should be defined for SE by mathematically describing the shape of the contact line in the 3-D space. For the current axi-symmetric geometry, the solid–water interfacial area can be obtained using Eq. 2.

$$\iint_{A_{s-w}} dA = \int_0^{2\pi} \int_{h-R}^{h-R\cos\varphi} R dz d\theta \quad (2)$$

where the bead is located above the plane of $z = 0$ and hs is the height of the bottom of the bead from the origin (see Fig. 1). In Eq. 2, φ , θ , and R are the angle from the bead's south pole, the longitude angle and the bead radius. Also, $h=R+hs$ is the bead center and it is $h = z + R\cos\varphi$ in terms of the bead coordinates. Integrating Eq. 2 with respect to z , one obtains,

$$\iint_{A_{s-w}} dA = \int_0^{2\pi} R(R - R\cos\varphi) d\theta \quad (3)$$

SE requires this integral to be defined in the Cartesian coordinates. This can be done by differentiating $\theta = \arctan\left(\frac{y}{x}\right)$ to obtain $d\theta = \frac{-ydx + xdy}{x^2 + y^2}$ where $x^2 + y^2 = R^2 - (z - hs - R)^2$, and by substituting it in Eq. 3 to obtain Eq. 4.

$$\iint_{A_{s-w}} dA = \int \frac{R}{2R + hs - z} (-ydx + xdy) \quad (4)$$

Eq. 4 is a line integral to be calculated along the edges of the missing face (i.e., the contact line) by SE.

With regard to the last term in Eq. 1 (energy term associated with the external body force on the droplet), assuming the gravity to be the only external body force (i.e., $f(z) = g$ and $U_{f(z)} = gz$), one can write $\iiint_w \rho_w g z dV = \iiint_{a-w} \rho_w g z dV + \iiint_{s-w} \rho_w g z dV$, in which the first and second terms on the right hand side are the volumes under the air–water and solid–water interfaces, respectively, and they should mathematically be defined for SE. For the volume integral under the air–water interface $\iiint_{a-w} \rho_w g z dV$, one can use the Divergence Theorem to transform this integral to a surface integral for a vector field $\frac{\rho_w g z^2}{2}$ having a divergence equals to the integrand of the volume integral, i.e.,

$$\iiint_{a-w} \rho_w g z dV = \iint \frac{\rho_w g z^2}{2} dA \quad (5)$$

For the volume integral under the solid–water interface $\iiint_{s-w} \rho_w g z dV$, one can use the following relationships to convert the volume integral to a line integral over the contact line.

$$\iiint_{s-w} \rho_w g z dV = \rho_w g \iiint_{z=0}^{z=h-R\cos\varphi} z dz \cos\varphi \sin\varphi R^2 d\varphi d\theta \quad (6)$$

Integrating Eq. 6 with respect to z and φ results in Eqs. 7 and 8, respectively.

$$\iiint_{s-w} \rho_w g z dV = \rho_w g \iiint_{\varphi=0}^{\varphi=\varphi} \left(\frac{h}{2}(h - R\cos\varphi)^2 - \frac{1}{2}(h - R\cos\varphi)^3 \right) R \sin\varphi d\varphi d\theta \quad (7)$$

$$\iiint_{s-w} \rho_w g z dV = \rho_w g \int_0^{2\pi} \left(\frac{h}{6}(z^3 - hs^3) - \frac{1}{8}(z^4 - hs^4) \right) d\theta \quad (8)$$

Finally, rewriting this equation in the Cartesian coordinate leads to Eq. 9.

$$\iiint_{s-w} \rho_w g z dV = \rho_w g \int \left(\frac{h}{6}(z^3 - hs^3) - \frac{1}{8}(z^4 - hs^4) \right) \frac{1}{R^2 - (z - h)^2} (-ydx + xdy) \quad (9)$$

With the above equations programmed in SE, one needs to define a set of constraints for the interfaces and contact lines to prevent any unrealistic solutions. For example, a constraint is needed to ensure that the droplet contact line remains on the surface of the bead during the energy minimization process (i.e., during droplet shape evolution). Therefore, with the bead placed above the plane of $z = 0$ (and hs representing the distance between the bottom of the bead and the origin), the constraint considered for the contact line (i.e., edges of the 6th face) will be $x^2 + y^2 + (z - hs - R)^2 = R^2$.

SE can calculate the volume of an enclosed shape automatically, but when the 6th face is not included in the simulations, a constraint is needed to ensure that the volume of the droplet is preserved during shape evolution. With the edges of the 6th face representing the contact line, SE considers the volume enclosed between the plane of $z = 0$ and the air–water interface as the droplet volume. However, the droplet volume is the volume between the solid–water and the air–water interfaces. To correct this, the volume between the plane of $z = 0$ and the bead surface (Eq. 10) must be calculated and added (with an opposite sign) to the volume calculated by SE.

$$\iiint_{s-w} dV = \iiint_{z=0}^{z=h-R\cos\varphi} dz \cos\varphi \sin\varphi R^2 d\varphi d\theta \quad (10)$$

Integrating Eq. 10 with respect to z and φ results in Eqs. 11 and 12, respectively.

$$\iiint_{s-w} dV = \iiint_{\varphi=0}^{\varphi=\varphi} (h(h - R\cos\varphi) - (h - R\cos\varphi)^2) R \sin\varphi d\varphi d\theta \quad (11)$$

$$\iiint_{s-w} dV = \int_0^{2\pi} \left(\frac{h}{2}(z^2 - hs^2) - \frac{1}{3}(z^3 - hs^3) \right) d\theta \quad (12)$$

Finally rewriting this equation in the Cartesian coordinate results in Eq. 13.

$$\iiint_{s-w} dV = \int \left(\frac{h}{2}(z^2 - hs^2) - \frac{1}{3}(z^3 - hs^3) \right) \frac{1}{R^2 - (z - h)^2} (-ydx + xdy) \quad (13)$$

Once the total energy of the system and the constraints are correctly programmed in SE, the simulation can start and continue until the energy of the system is minimized (with the constraints enforced during the iterations).

Once the total energy of the system is formulated, a SE code will need to be developed. In this code, all parameters such as droplet volume, surface tensions, and droplet densities will need to be defined. These parameters do not have to be constant values; they can vary with position as field functions (e.g., magnetic force can be defined as $f(z)$). A second section of the code will define the constraints. The constraints are needed to ensure that the initial droplet evolves into a physically-meaningful realistic shape. For example, the solid–liquid face should always remain on the surface of the bead and therefore a constraint such

as $x^2 + y^2 + z^2 = R^2$ is needed. In the constraints section, corrections can be made to droplet volume or surface area if needed. Additional forms of energy (other than those associated with surface tension or gravity), e.g., from a magnetic or electric force can also be defined in this section. The third section of the code will define the initial geometry of the droplet, and it will be followed by a section that will specify what algorithm should be used to evolve the shape of the droplet.

Fig. 2a compare the surface energy of the air–water interface with that of the solid–water interface (obtained indirectly as explained earlier) and the energy associated with the gravitational potential for a pendant droplet with a volume of 4 μL on a solid bead with a diameter of 4 mm and a YLCA of 95 degrees (see Video 1). The inset figures show how the 3-D shape of the droplet evolves through iterations and eventually converges to an equilibrium shape. The droplet is assumed to be a water-based ferrofluid (for the results to be compared with the experiment in the next section) with a surface tension of $\sigma_{a-wf} = 64\text{mN/m}$. It can be seen that the energy of the air–water interface is significantly higher than those associated the gravitational force and the solid–water interface (note that air–water interface is much larger than the

solid–water interface as shown in Fig. 2b).

Supplementary material related to this article can be found online at [doi:10.1016/j.colsurfa.2021.127418](https://doi.org/10.1016/j.colsurfa.2021.127418).

2.2. Method 2

In this new approach, we use a 6-faced cube to represent the initial shape of the droplet (as opposed to the 5-faced cube of the previous subsection). The 6th face is the solid–water interface. The interfacial tension of this face is not a quantity often reported in tables, but it can be obtained from the Young–Laplace equation $-\sigma_{a-w}\cos\theta_w^{YL} = \sigma_{a-w} - \sigma_{s-a}$ and used in Eq. 1. For simplicity in this work, we define $\Delta\sigma_{s-w} = \sigma_{s-a} - \sigma_{s-w}$, and assign it to the 6th face. Therefore, the total energy of the air–water–solid system (Eq. 1) can be rewritten as,

$$E_t = \sigma_{a-w}A_{a-w} + \Delta\sigma_{s-w}A_{s-w} + \iiint_w \rho_w U_f(z) dV \quad (14)$$

This simple modification to Eq. 1 allows us to circumvent the need for deriving mathematical expressions for the solid–water contact area (Eqs. 2–4), the line-integral transformation of Eqs. 6–9, and the droplet volume correction of Eqs. 10–13. Note that the aforementioned constraint of $x^2 + y^2 + (z - h)^2 = R^2$ should still be considered for all the vertices of the 6th face.

Fig. 3a compares the solid–water energy of the system obtained using Method 1 and Method 2 (see Video 2) for the same ferrofluid droplet

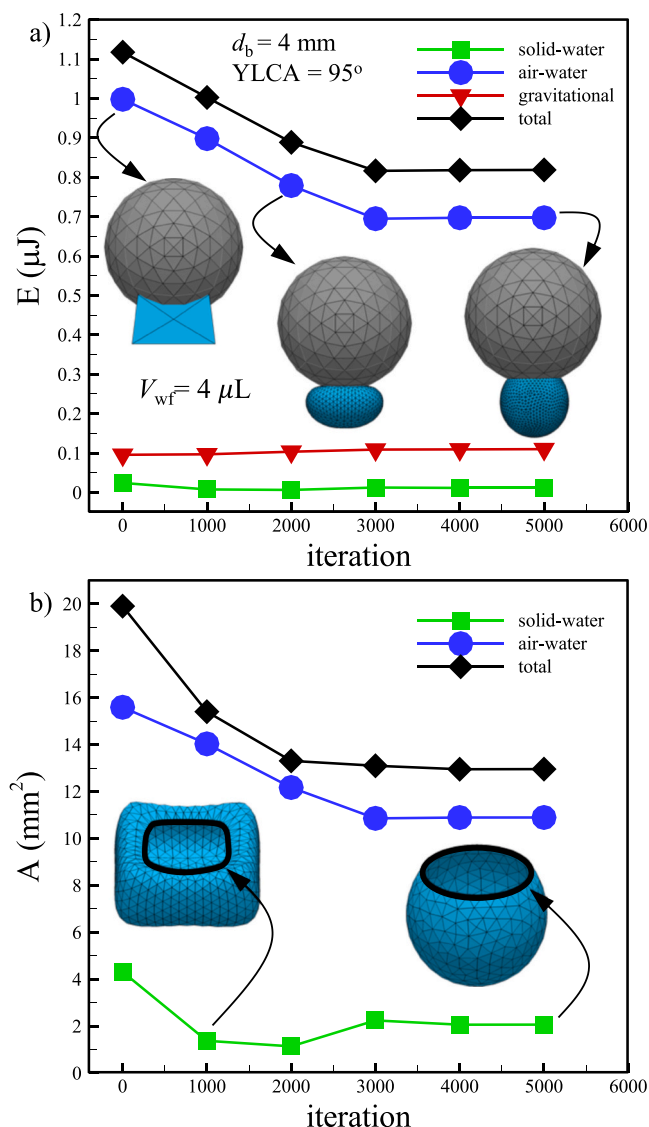


Fig. 2. Total energy of the system consisting of solid–water (i.e., water-based ferrofluid) energy, air–water energy, and gravitational energy are plotted in (a) as the droplet shape evolves. Air–water, solid–water, and total interfacial areas are plotted in (b) vs. iterations. Droplet volume, sphere diameter, solid YLCA (with the water-based ferrofluid) are 4 μL , 4 mm, and 95°, respectively.

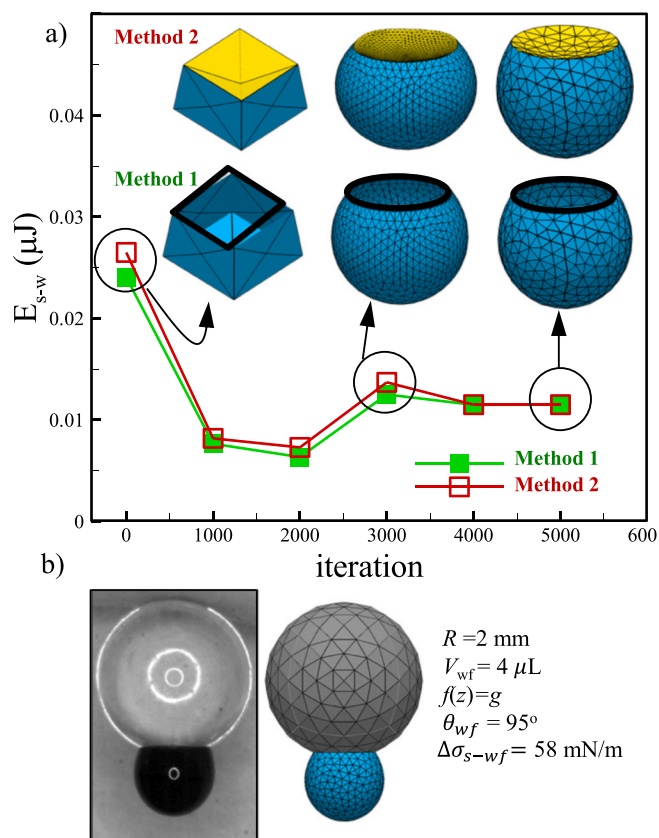


Fig. 3. Solid–water interfacial energy E_{s-w} is calculated using Method 1 and Method 2 and plotted vs. iterations in (a). Yellow and black colors represent the 6th face and the droplet contact line, respectively. SE simulation results obtained from both Methods 1 and 2 (identical) are shown in (b) next to their experimental counterpart obtained using a water-based ferrofluid (EMG 508) with a volume of 4 μL on a coated glass bead with a radius of 2 mm. The YLCA between the water-based ferrofluid and coated bead was obtained experimentally to be 95 degrees. (For interpretation of the references to colour in this figure legend, the reader is referred to the web version of this article.)

shown previously in Fig. 2. The droplet profile evolution and the solid–water energy are slightly different in the beginning, but they eventually converge to the same point. This is also true for other terms in the equation. The yellow face is the sixth face that is considered in the new simulation method as the figure inset shows the droplet profile evolution using the conventional and the proposed methods. Fig. 3b shows a good agreement between droplet profiles obtained from the experiment and the SE simulation (using either of the methods) when the droplet is under gravity. Note that $\Delta\sigma_{s-w} = 58\text{ mN/m}$ was used to simulate a YLCA of 95° for the water-based ferrofluid droplet on the bead using Method 2.

Supplementary material related to this article can be found online at doi:10.1016/j.colsurfa.2021.127418.

Fig. 4 presents an example where the proposed model allowed us to conduct a set of simulations that would otherwise be quite challenging. In this figure, the pendant droplet of Fig. 2 is exposed a spatially non-uniform body force, i.e., a magnetic repulsion force [54]. For this simulation, the gravitational energy term of Eq. 1 was modified as follows. Consider a spatially-varying magnetic flux density in the z-direction given as $B = az^2 + bz + c$, where a (T/m^2), b (T/m), and c (T) are constant numbers, and z is the distance between the magnet and the droplet (see [54] for more details). The force per unit mass acting on the ferrofluid droplet can be obtained from Eq. 15,

$$f(z) = \frac{\Delta\chi}{\rho_w\mu_0} B\nabla B \quad (15)$$

where $\Delta\chi$ is the difference between the magnetic susceptibility of the aqueous droplet and the ferrofluid nanoparticles, and $\mu_0 = 4\pi \times 10^{-7}$ H/m is the permeability of the free space. Eq. 15 can be used to obtain a potential function for the magnetic force, as

$$U_{f(z)} = \frac{\Delta\chi}{\rho_w\mu_0} \left(a^2 z^4 / 2 + abz^3 + (2ac + b^2)z^2 / 2 + bc z \right) \quad (16)$$

Substituting $U_{f(z)}$ in $\iiint_w \rho_w U_{f(z)} dV$ and transforming the volume integral to the surface integral using the Divergence Theorem results in:

$$\iiint_w U_{f(z)} dV = \iint_w \rho_w \frac{\Delta\chi}{\rho_w\mu_0} \left(a^2 z^5 / 10 + abz^4 / 4 + (2ac + b^2)z^3 / 6 + bc z^2 / 2 \right) dA \quad (17)$$

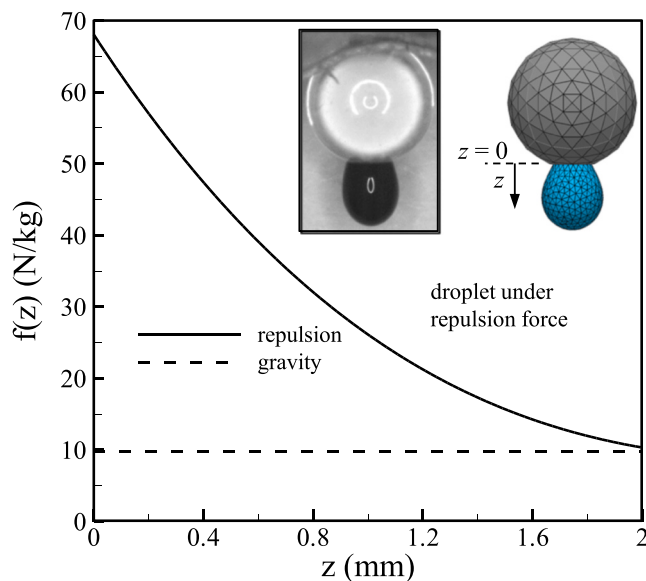


Fig. 4. Variations of gravitational and magnetic (repulsion) accelerations are plotted across the droplet length for a droplet with a volume of $4\ \mu\text{L}$ placed on a coated glass bead with a radius of 2 mm coated and a YLCA of 95° .

Note that with our proposed modeling approach, the above surface integral no longer needs to be converted to a line integral. The inset in Fig. 4 compares the simulated droplet shape with its experimental counterpart under an average weighted force per mass of about $f = 29\ \frac{\text{N}}{\text{kg}}$. Our experiments were conducted using ferrofluid droplets so that the droplet shape could be manipulated by a permanent magnet (to enhance or cancel the gravity). Readers are referred to our previously publications for additional details about these experiments [49,52,54]. Despite the small differences (due mostly to the simplifying assumptions considered in the simulations) the agreement between the experimental and computational results are reasonably good.

3. Simulating a two-phase droplet on a curved surface

We discuss simulation of two-phase droplets comprised of immiscible polar and non-polar liquids using SE in this section. A two-phase compound droplet can be produced, for instance, by adding a small amount of oil to a water droplet. In this case, the oil (having a surface tension smaller than that of water) will fully- or partially-cloak the water droplet depending on the oil surface tension relative to that of water, the method by which the oil was added, and whether or not the droplet is under the influence of an external body force. In the absence of external forces, the spreading coefficient $S = \sigma_w - \sigma_o - \sigma_{w-o}$ can be used to estimate whether cloaking will be partial ($S < 0$) or complete ($S > 0$) [57–66].

3.1. Partially cloaked droplets ($S < 0$)

Fig. 5a shows a pendant water droplet partially cloaked with oil. In this case, oil's surface tension is relatively high (still less than that of water), i.e., $\sigma_{a-w} < \sigma_{a-o} + \sigma_{w-o}$, and it is added to the droplet from below. With partially-cloaked water droplets, it is likely that the solid–water area and the air–water interfacial tension values do not change because of the added oil. Extending the application of Method 2 (Section 2.2), the total energy of the air–water–oil–solid system can therefore be represented by Eq. 1 after some modifications, i.e.,

$$E_t = \sigma_{a-w}A_{a-w} + \Delta\sigma_{s-w}A_{s-w} + \sigma_{a-o}A_{a-o} + \sigma_{w-o}A_{w-o} + \iiint_w \rho_w g z dV + \iiint_o \rho_o g z dV + \iiint_o \rho_o U_{f(z)} dV \quad (18)$$

where the water droplet is under gravity but the oil (ferrofluid here) is also under the influence of a magnetic body force $f(z)$. Similar to the case of the single-phase droplets, energy terms of $\iiint_w \rho_w g z dV$, $\iiint_o \rho_o g z dV$ and $\iiint_o \rho_o U_{f(z)} dV$ should be defined for SE for the problem at hand. In addition, the constraint $x^2 + y^2 + (z - h_s - R)^2 = R^2$ needs to be imposed to any fluid that comes into contact with the solid surface. For this case ($S < 0$), the SE simulations should start with cubic droplets placed on top of each other. Fig. 5b shows a $4\ \mu\text{L}$ water droplet partially cloaked by a $1.3\ \mu\text{L}$ oil-based ferrofluid under the influence of gravity (imaged experimentally and simulated using SE, see Videos 3 and 4). The water surface tension, density, and YLCA with the solid surface were assumed to be $72\ \text{mN/m}$, $998\ \text{kg/m}^3$, and 107° , respectively. For the simulations, a solid–water tension of $\Delta\sigma_{s-w} = 21\ \text{mN/m}$ was used in Eq. 18 to match the experimental YLCA of 107° . The oil surface tension and density were chosen to be $32\ \text{mN/m}$ and $1060\ \text{kg/m}^3$, respectively. Red, light blue, and dark blue represent oil, water, and water–oil interface, respectively. For the case of water droplets submerged in a bath of oil, the empirical correlation in Eq. 19 can be used to estimate the water–oil interfacial tension [67].

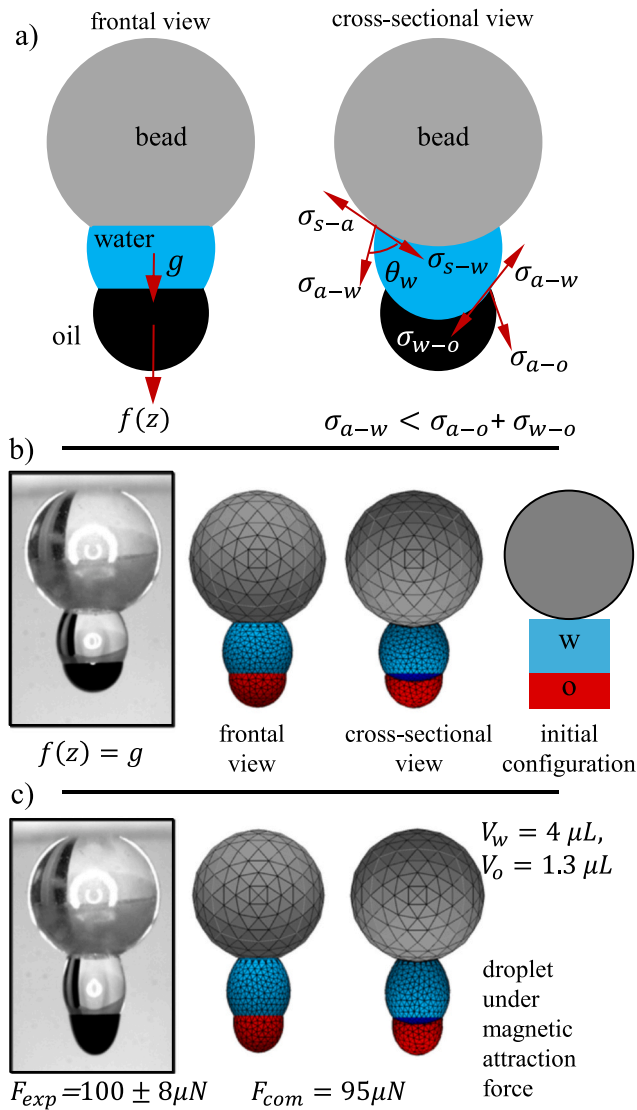


Fig. 5. Schematic drawings for a water droplet partially cloaked ($S>0$) with an oil-based ferrofluid (APG 2133) are shown in (a) from the frontal and cross-sectional views. Droplet shapes obtained experimentally and numerically are compared in (b) and (c) under gravity and downward magnetic attraction force, respectively. Colors light blue, red, and blue represent air–water interface, oil–air interface, and water–oil interface, respectively. (For interpretation of the references to colour in this figure legend, the reader is referred to the web version of this article.)

$$\sigma_{w-o} = \frac{\cosh\left(\frac{\sigma_w}{k}\right)\sigma_w^{1-m} - \cosh\left(\frac{\sigma_o}{k}\right)\sigma_o^{1-m}}{\cosh\left(\frac{\sigma_w + \sigma_o - c\sigma_w\sigma_o^{1-n}}{k}\right)(\sigma_w + \sigma_o - c\sigma_w\sigma_o^{1-n})^{-m}} \quad (19)$$

where $m = 0.938$, $n = 0.949$, $c = 0.837$ and $k = 42.121 \text{ mN/m}$. Using the above equation, we obtain an interfacial tension of $\sigma_{w-o} = 46 \text{ mN/m}$ for the water–oil interface. Note that, while Eq. 19 is very valuable for its universal application, it only provides a rough estimate for the water–oil interfacial tension (the experimental data used to produce Eq. 19 had root mean squared errors as high as 4.14 mN/m). Fig. 5c shows the same droplet as in Fig. 5b but when a downward magnetic force is applied to the ferrofluid (in addition to the force of gravity). For the case shown in this figure, the force acting on the droplet was obtained from the simulations to be $F_{comp} = 95 \mu\text{N}$ in good agreement with the total body force applied to the droplet experimentally ($F_{exp} = 100 \pm 8 \mu\text{N}$). The example presented in Fig. 4 is followed here to calculate the energy due to the

magnetic attraction force (i.e. $\iiint_0 \rho_o U_{f(z)} dV$) in Eq. 18 (see [54] for more details on the experimental method and magnetic attraction and repulsion forces). The Bond number ($Bo = \frac{\rho g R^2}{\sigma_{a-w}}$) and Capillary length ($l_{ca} = \sqrt{\frac{\sigma_{a-w}}{\rho g}}$) for this droplet were found to be 0.54 and 2.71 mm , respectively.

Supplementary material related to this article can be found online at [doi:10.1016/j.colsurfa.2021.127418](https://doi.org/10.1016/j.colsurfa.2021.127418).

3.2. Fully cloaked droplets ($S<0$)

When the oil surface tension is low, i.e., $\sigma_{a-w} > \sigma_{a-o} + \sigma_{w-o}$, it develops a thin film that fully covers the surface of the water droplet (i.e., fully cloaks the droplet) as shown in Fig. 6a. The thickness of the cloaking oil-film depends on many factors, but it can be as small as 20 nm [13]. It is therefore impossible for us to directly simulate the

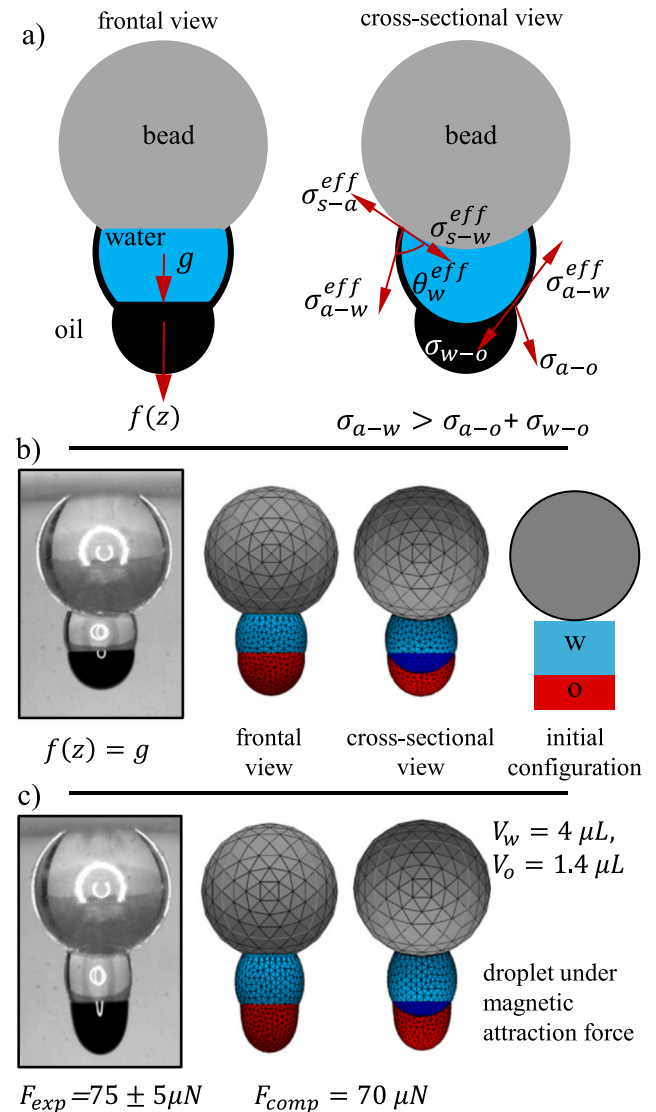


Fig. 6. Schematic drawings for a water droplet full cloaked ($S<0$) with an oil-based ferrofluid (EMG 911) are shown in (a) from the frontal and cross-sectional views. Droplet shapes obtained experimentally and numerically are compared in (b) and (c) under gravity and downward magnetic attraction force, respectively. Colors light blue, red, and blue represent air–water interface, oil–air interface, and water–oil interface, respectively. (For interpretation of the references to colour in this figure legend, the reader is referred to the web version of this article.)

nanometer-sized film and the millimeter-sized water droplet in the same computational domain using SE. One has to therefore consider an *effective* surface tension value for the oil-cloaked air–water interface σ_{a-w}^{eff} as well as an *effective* contact angle for the air–water interface at the air–water–solid contact points θ_w^{eff} [63–66]. Likewise, an *effective* solid–water surface tension difference $\Delta\sigma_{s-w}^{eff} = \sigma_{s-w}^{eff} - \sigma_{s-a}^{eff}$ should be used in SE when using simulation Method 2. Total energy of the air–water–oil–solid system can therefore be represented by Eq. 18 after some modifications, i.e.,

$$E_t = \sigma_{a-w}^{eff} A_{a-w} + \Delta\sigma_{s-w}^{eff} A_{s-w} + \sigma_{a-o} A_{a-o} + \sigma_{w-o} A_{w-o} + \iiint_w \rho_w g z dV + \iiint_o \rho_o g z dV + \iiint_o \rho_o U_f(z) dV \quad (20)$$

SE simulations should again start with cubic droplets placed on top of one another. Fig. 6b shows a 4 μ L water droplet partially cloaked with a 1.4 μ L oil ferrofluid droplet under gravity (imaged experimentally and simulated using SE, see Videos 5 and 6). For these simulations, an effective water surface tension of $\sigma_{a-w}^{eff} = 64$ mN/m and an effective solid–water surface tension difference of $\Delta\sigma_{s-w}^{eff} = 18$ mN/m were used in Eq. 20. The selected value for the effective surface tension depends on the thickness of the oil film and on its surface tension. For instance, in Ref. [68], effective surface tension values of $\sigma_{a-w}^{eff} = 70.4 \pm 4$ mN/m and $\sigma_{a-w}^{eff} = 57.5 \pm 3.5$ mN/m were obtained for a water droplet coated with fumed fluorosilica particles and with a thin layer of silicone oil, respectively. The authors in Ref. [68] used a simple puddle height method to calculate these effective surface tensions. The oil surface tension and density were considered to be 18 mN/m and 890 kg/m³, respectively. The water–oil surface tension was obtained from Eq. 19 to be $\sigma_{w-o} = 48$ mN/m. Fig. 6c shows the same droplet as in Fig. 6b but when a magnetic force is applied to the ferrofluid (in addition to the force of gravity). The force acting on the droplet was obtained from the simulations to be $F_{comp} = 70 \mu$ N in good agreement with the total body force applied to the droplet experimentally ($F_{exp} = 75 \pm 5 \mu$ N). Using this effective surface tension for the water droplet, the Bond number and Capillary length for this droplet were found to be 0.61 and 2.55 mm, respectively.

Supplementary material related to this article can be found online at doi:10.1016/j.colsurfa.2021.127418.

3.3. Other configurations for fully cloaked droplets ($S < 0$)

It should be noted that, a fully cloaking oil film may also climb up the bead (depending on the bead's oleophobicity), especially when the droplet is cloaked with excessive amounts of oil (see Fig. 7a). In such cases, the cloaking oil breaks up into two volumes plus a thin film connecting them. To simulate such droplets, an additional term $\Delta\sigma_{s-o} A_{s-o}$ should be added to Eq. 18 in addition to considering the effective surface tension for the air–water interface covered by the thin film in the middle. The total energy for the air–water–oil–solid system can therefore be written as,

$$E_t = \sigma_{a-w}^{eff} A_{a-w} + \Delta\sigma_{s-w}^{eff} A_{s-w} + \sigma_{a-o} A_{a-o} + \sigma_{w-o} A_{w-o} + \Delta\sigma_{s-o} A_{s-o} + \iiint_w \rho_w g z dV + \iiint_o \rho_o g z dV + \iiint_o \rho_o U_f(z) dV \quad (21)$$

For this case, SE simulations should start with cubic droplets placed on top of one another but the bottom cubic droplet (i.e. water droplet) should be partially inside a bigger cubic droplet (see Fig. 7b). Fig. 7b shows a 4 μ L water droplet fully cloaked with a 1.4 μ L oil ferrofluid droplet under gravity (see Videos 7 and 8). The effective water–oil surface tension is taken to be $\sigma_{a-w}^{eff} = 60$ mN/m for the simulations. Note in this case that, the effective solid–water surface tension

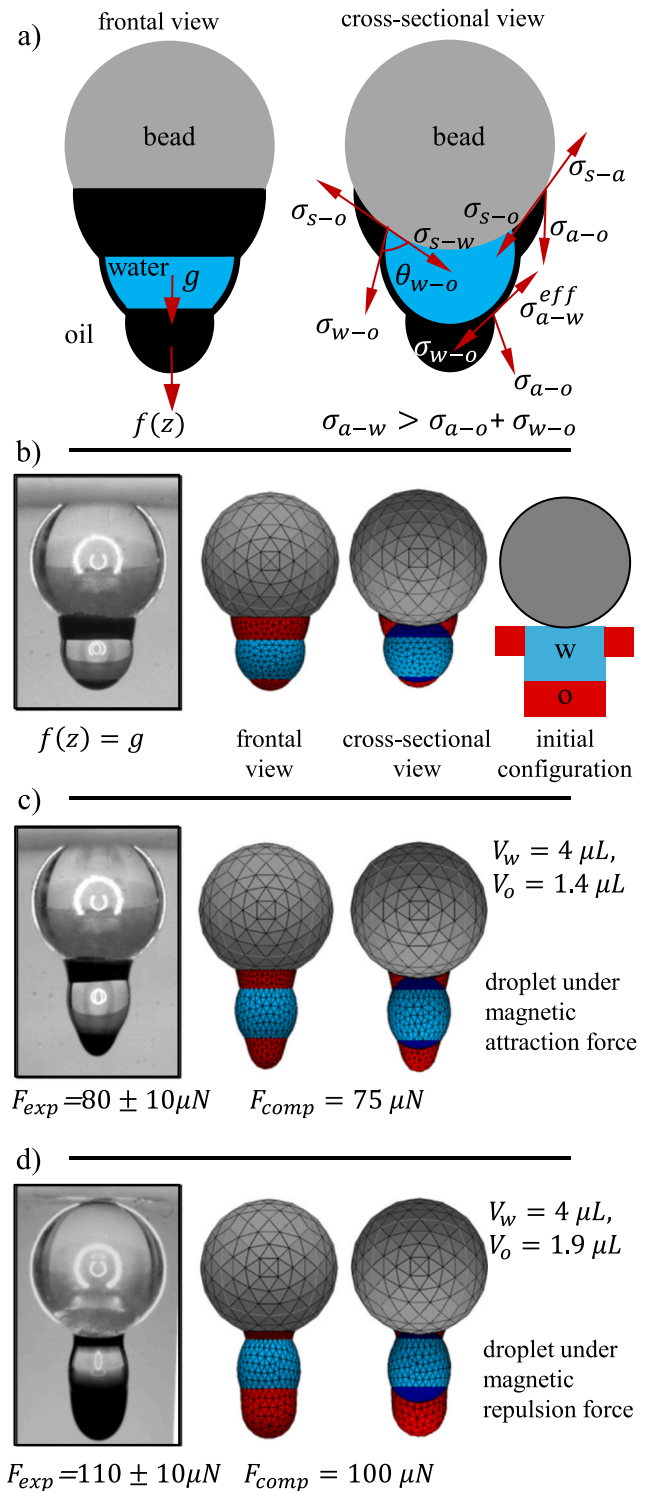


Fig. 7. Schematic drawings for a water droplet full cloaked ($S < 0$) with an oil-based ferrofluid (EMG 911) are shown in (a) from the frontal and cross-sectional views. Droplet shapes obtained experimentally and numerically are compared in (b), (c), and (d) under gravity, downward magnetic attraction force, and downward magnetic repulsion force, respectively. Colors light blue, red, and blue represent air–water interface, oil–air interface, and water–oil interface, respectively. Note that ferrofluid volume is different in each case. (For interpretation of the references to colour in this figure legend, the reader is referred to the web version of this article.)

difference $\Delta\sigma_{s-w}^{eff}$ should not be considered (Eq. 21). This is because the part of the water droplet close to the solid surface is fully immersed in the oil. In this case, the contact angle for an immersed droplet θ_{w-o} can be calculated using Young's equation as,

$$\cos\theta_{w-o} = \frac{\sigma_{a-w}\cos\theta_w - \sigma_{a-o}\cos\theta_o}{\sigma_{w-o}} \quad (22)$$

Supplementary material related to this article can be found online at doi:10.1016/j.colsurfa.2021.127418.

Using $\sigma_{a-w} = 72\text{mN/m}$ for the air–water surface tension, $\theta_w = 107^\circ$ for the water contact angle in air, $\theta_o = 45^\circ$ for the oil contact angle with solid, $\sigma_{a-o} = 18\text{mN/m}$ for the oil surface tension, and $\sigma_{w-o} = 18\text{mN/m}$ for the water–oil interfacial tension, one obtains $\theta_{w-o} = 137^\circ$. Because the contact angle is not an input in Method 2, an equivalent solid–water surface tension difference of $\Delta\sigma_{s-w} = 0.035\text{N/m}$ was used in these simulations. Fig. 7c shows the same droplet as in Fig. 7b but when a magnetic force is also applied to the ferrofluid. The force acting on the droplet was obtained from the simulations to be $F_{comp} = 75\mu\text{N}$ in good agreement with the total body force applied to the droplet experimentally ($F_{exp} = 80 \pm 10\mu\text{N}$). In Fig. 7d, the oil volume is increased to $1.9\mu\text{L}$. In this case we added a downward magnetic repulsion force to the ferrofluid (see [54] for more information about magnetic repulsion and attraction forces and their attributes). In this case, the simulated and measured forces were found to be $F_{comp} = 100\mu\text{N}$ and $F_{exp} = 110 \pm 10\mu\text{N}$, respectively, and obviously in good general agreement with one another. Using this effective surface tension for the water droplet, the Bond number and Capillary length for this droplet were found to be 0.65 and 2.47 mm, respectively.

While the examples presented in this section are for the specific case of a pendant compound droplet on a spherical bead, the same simulation strategy can be utilized to model the interactions between multiphase droplets of different compositions and solid surfaces of different morphologies using SE program. The examples given here also illustrate how SE can be used to simulate a compound droplet in a condition where only one of the two constituting phases responds to an external body force, and that the body force can be spatially non-uniform (unlike gravity). The information presented in this paper can, for instance, be used to simulate the shape of a droplet on a lubricant-infused surface [12–20]. Similarly, an effective surface tension should be considered for the water droplet on a lubricant-infused surface as a thin cloak of oil around the droplet cannot be directly simulated in SE [15,16,63]. This of course requires detailed information about the wetting properties of the solid and liquid phases involved as well as the steps by which the compound droplet was produced.

4. Conclusions

Interested in quantifying the force required to detach a compound droplet (e.g., an oil-coated water droplet) from a curved surface, we developed an easy-to-implement simulation strategy to use Surface Evolver (SE) program for the complicated four-phase (air, water, oil, and solid) interfacial problem at hand. Such simulations improve our quantitative understanding of how multiphase droplets generally interact with surfaces of different morphologies for a variety of industrial applications, including but not limited to, self-cleaning, droplet filtration, and microfluidics.

SE simulation of a single-phase droplet generally starts by considering a 5-faced cubic droplet with the 6th face (solid–liquid contact area) defined and formulated for the solver using droplet contact angle along the contact line (the edges of the 6th face). An alternative approach is to consider a 6-faced cubic droplet and to specify a solid–water surface tension for the 6th face. The latter is significantly simpler mathematically, and also allows one to use SE to simulate multiphase droplets on solid surfaces of arbitrary curvatures, and in the presence of a non-uniform external body force. The multiphase droplet considered

in this work is a water droplet cloaked with oil-based ferrofluids of high (partially cloaking) or low (fully cloaking) surface tension. The concept of effective surface tension and effective contact angle is discussed in the context of existing literature and is used here in conducting numerical simulations for compound droplets. Good general agreement was observed between the results of our numerical simulations and those obtained from experiment.

CRediT authorship contribution statement

HVT defined the problem statement and proposed a solution strategy. MJ conducted the experiments and developed the simulations. MJ and HVT discussed and analyzed the results and wrote the paper jointly.

Declaration of Competing Interest

The authors declare that they have no known competing financial interests or personal relationships that could have appeared to influence the work reported in this paper.

Acknowledgement

The authors acknowledge the National Science Foundation CBET program (1402655) for financial support.

References

- [1] E.A. Bormashenko, *Wetting of Real Surfaces*; Walter de Gruyter, 2013.
- [2] J.W. Drelich, Contact angles: from past mistakes to new developments through liquid–solid adhesion measurements, *Adv. Colloid Interface Sci.* 267 (2019) 1.
- [3] D. Wang, Y. Jiang, Z. Zhu, W. Yin, K. Asawa, C.-H. Choi, J.W. Drelich, Contact line and adhesion force of droplets on concentric ring-textured hydrophobic surfaces, *Langmuir* 36 (2020) 2622.
- [4] S.J. Lee, J. Hong, K.H. Kang, I.S. Kang, S.J. Lee, Electrowetting-induced droplet detachment from hydrophobic surfaces, *Langmuir* 30 (2014) 1805.
- [5] A. Cavalli, D.J. Preston, E. Tio, D.W. Martin, N. Miljkovic, E.N. Wang, F. Blanchette, J.W.M. Bush, Electrically induced drop detachment and ejection, *Phys. Fluids* 28 (2016), 022101.
- [6] C.T. Burkhart, K.L. Maki, M.J. Schertzer, Coplanar electrowetting-induced droplet detachment from radially symmetric electrodes, *Langmuir* 36 (2020) 8129.
- [7] S. Jung, M. Dorrestijn, D. Raps, A. Das, C.M.; Megaridis, D. Poulikakos, Are superhydrophobic surfaces best for icephobicity? *Langmuir* 27 (2011) 3059.
- [8] S. Nath, J.B. Boreyko, On localized vapor pressure gradients governing condensation and frost phenomena, *Langmuir* 32 (2016) 8350.
- [9] R. Tadmor, P. Bahadur, A. Leh, H.E. N'guessan, R. Jaini, L. Dang, Measurement of lateral adhesion forces at the interface between a liquid and a substrate, *Phys. Rev. Lett.* 103 (2009), 266101.
- [10] B. Bharat, J.Y. Chae, Natural and biomimetic artificial surfaces for superhydrophobicity, self-cleaning, low adhesion, and drag reduction, *Prog. Mater. Sci.* 56 (2011) 1.
- [11] R. Tadmor, R. Das, S. Gulec, J. Liu, H.E. Nguessan, M. Shah, P.S. Wasnik, S. B. Yadav, Solid-liquid work of adhesion, *Langmuir* 33 (2017) 3594.
- [12] J.D. Smith, R. Dhiman, S. Anand, E. Reza-Garduno, R.E. Cohen, G.H. McKinley, K. K. Varanasi, Droplet mobility on lubricant-impregnated surfaces, *Soft Matter* 9 (2013) 1772.
- [13] F. Schellenberger, J. Xie, N. Encinas, A. Hardy, M. Klapper, P. Papadopoulos, H. J. Butt, D. Vollmer, Direct observation of drops on slippery lubricant-infused surfaces, *Soft Matter* 11 (2015) 7617.
- [14] S. Sett, X. Yan, G. Barac, L.W. Bolton, N. Miljkovic, Lubricant-infused surfaces for low-surface-tension fluids: promise versus reality, *ACS Appl. Mater. Interfaces* 9 (2017) 36400–36408.
- [15] M.J. Kreder, D. Daniel, A. Tetreault, Z. Cao, B. Lemaire, J.V.I. Timonen, J. Aizenberg, Film dynamics and lubricant depletion by droplets moving on lubricated surfaces, *Phys. Rev. X* 8 (2018), 031053.
- [16] G. McHale, B.V. Orme, G.G. Wells, R. Ledesma-Aguilar, Apparent contact angles on lubricant-impregnated surfaces/slips: from superhydrophobicity to electrowetting, *Langmuir* 35 (2019) 4197.
- [17] M. Sharma, P.K. Roy, J. Barman, K. Khare, Mobility of aqueous and binary mixture drops on lubricating fluid-coated slippery surfaces, *Langmuir* 35 (2019) 7672.
- [18] M. Villegas, Y. Zhang, N. Abu Jarad, L. Soleymani, T.F. Didar, Liquid-infused surfaces: a review of theory, design, and applications, *ACS Nano* 13 (2019) 8517.
- [19] J. Suna, P.B. Weisensee, Microdroplet self-propulsion during dropwise condensation on lubricant-infused surfaces, *Soft Matter* 15 (2019) 4808.
- [20] S. Adera, J. Alvarenga, A.V. Shneidman, C.T. Zhang, A. Davitt, J. Aizenberg, Depletion of lubricant from nanostructured oil-infused surfaces by pendant condensate droplets, *ACS Nano* 14 (2020) 8024.
- [21] O.V. Pyankov, I.E. Agranovski, R. Huang, B.J. Mullins, Removal of biological aerosols by oil coated filters, *Clean. Soil Air Water* 36 (7) (2008) 609.

- [22] R. Mead-Hunter, A.J.C. King, B.J. Mullins, Aerosol-mist coalescing filters – a review, *Sep. Purif. Technol.* 133 (2014) 484–506.
- [23] P.S. Kulkarni, S.U. Patel, G.G. Chase, Layered hydrophilic/hydrophobic fiber media for water-in-oil coalescence, *Sep. Purif. Technol.* 85 (2012) 157.
- [24] D. Kampa, S. Wurster, J. Buzengeiger, J. Meyer, G. Kasper, Pressure drop and liquid transport through coalescence filter media used for oil mist filtration, *Int. J. Multiph. Flow* 58 (2014) 313.
- [25] T.K. Muller, J. Meyer, E. Thebault, G. Kasper, Impact of an oil coating on particle deposition and dust holding capacity of fibrous filters, *Powder Technol.* 253 (2014) 247.
- [26] C.J. Hotz, R. Mead-Hunter, T. Becker, A.J.C. King, S. Wurster, G. Kasper, B. J. Mullins, Detachment of droplets from cylinders in flow using an experimental analogue, *J. Fluid Mech.* 771 (2015) 327–340.
- [27] X. Tian, H. Jin, J. Sainio, R.H.A. Ras, O. Ikkala, Droplet and fluid gating by biomimetic Janus membranes, *Adv. Funct. Mater.* 24 (2014) 6023.
- [28] P. Gupta, B. Kandasubramanian, Directional fluid gating by Janus membranes with heterogeneous wetting properties for selective oil–water separation, *ACS Appl. Mater. Interfaces* 9 (2017) 19102.
- [29] H.C. Yang, Y. Xie, J. Hou, A.K. Cheetham, V. Chen, S.B. Darling, Janus membranes: creating asymmetry for energy efficiency, *Adv. Mater.* 30 (2018), 1801495.
- [30] Y.M. Lin, C. Song, G.C. Rutledge, Direct three-dimensional visualization of membrane fouling by confocal laser scanning microscopy, *ACS Appl. Mater. Interfaces* 11 (2019) 17001.
- [31] E. Gauthier, T. Hellstern, I.G. Gauthier, J. Benziger, Drop detachment and motion on fuel cell electrode materials, *ACS Appl. Mater. Interfaces* 4 (2012) 761.
- [32] M. Andersson, A. Mularczyk, A. Lamibrac, S.B. Beale, J. Eller, W. Lehnert, F. N. Buchi, Modeling and synchrotron imaging of droplet detachment in gas channels of polymer electrolyte fuel cells, *J. Power Sources* 404 (2018) 159.
- [33] J. Ju, H. Bai, Y. Zheng, T. Zhao, R. Fang, L. Jiang, A multi-structural and multi-functional integrated fog collection system in cactus, *Nat. Commun.* 3 (2012) 1247.
- [34] W. Shi, M.J. Anderson, J.B. Tulkoff, B.S. Kennedy, J.B. Boreyko, Fog harvesting with harps, *ACS Appl. Mater. Interfaces* 10 (14) (2018) 11979.
- [35] M. Samaha, F.O. Ochanda, H.V. Tafreshi, G.C. Tepper, M. Gad-el-Hak, In situ, noninvasive characterization of superhydrophobic coatings, *Rev. Sci. Instrum.* 82 (2011), 045109.
- [36] T.M. Bucher, B. Emami, H.V. Tafreshi, M. Gad-el-Hak, G.C. Tepper, Modeling resistance of nanofibrous superhydrophobic coatings to hydrostatic pressures: the role of microstructure, *Phys. Fluids* 24 (2012), 022109.
- [37] R. Mead-Hunter, A.J.C. King, B.J. Mullins, Plateau Rayleigh instability simulation, *Langmuir* 28 (17) (2012), 6731–6733.
- [38] R. Mead-Hunter, A.J.C. King, G. Kasper, B.J. Mullins, Computational fluid dynamics (CFD) simulation of liquid aerosol coalescing filters, *J. Aerosol Sci.* 61 (2013) 36.
- [39] H. Yu, L. Goldsworthy, M. Ghiji, P.A. Brandner, V. Garaniya, A parallel volume of fluid-Lagrangian Parcel Tracking coupling procedure for diesel spray modelling, *Comput. Fluids* 150 (2017), 46–46.
- [40] W. Edelbauer, F. Birkhold, T. Rankel, Z. Pavlovic, P. Kolar, Simulation of the liquid break-up at an AdBlue injector with the volume-of-fluid method followed by off-line coupled Lagrangian particle tracking, *Comput. Fluids* 157 (2017) 294.
- [41] O. Desjardins, V. Moureau, H. Pitsch, An accurate conservative level set/ghost fluid method for simulating turbulent atomization, *J. Comput. Phys.* 227 (2008) 8395–8841.
- [42] S. Wang, O. Desjardins, 3D numerical study of large-scale two-phase flows with contact lines and application to drop detachment from a horizontal fiber, *Int. J. Multiph. Flow* 101 (2018) 35–46.
- [43] J. Carmeliet, L. Chen, Q. Kang, D. Derome, Beyond-cassie mode of wetting and local contact angles of droplets on checkboard-patterned surfaces, *Langmuir* 33 (2017) 6192–6200.
- [44] S.H. Lee, S.W. Son, H.Y. Choi, S.H. Park, M.Y. Ha, A numerical study on the separation of droplet on the heterogeneous surface, *Comput. Fluids* 152 (2017) 231–247.
- [45] S. Abishek, R. Mead-Hunter, A.J.C. King, B.J. Mullins, Capture and re-entrainment of microdroplets on fibers, *Phys. Rev. E* 100 (2019), 042803.
- [46] E. Ezzatneshan, R. Goharimehr, Study of spontaneous mobility and imbibition of a liquid droplet in contact with fibrous porous media considering wettability effects, *Phys. Fluids* 32 (2020), 113303.
- [47] K.A. Brakke, The surface evolver and the stability of liquid surfaces, *Philos. Trans. R. Soc. A-Math. Phys. Eng. Sci.* 354 (1996) 2143.
- [48] D. Chatain, D. Lewis, J.P. Baland, W.C. Carter, Numerical analysis of the shapes and energies of droplets on micropatterned substrates, *Langmuir* 22 (2006) 4237–4243.
- [49] M.M. Amrei, D.G. Venkateshan, N. D'Souza, J. Atulasimha, H.V. Tafreshi, Novel approach to measuring the droplet detachment force from fibers, *Langmuir* 32 (2016) 13333.
- [50] M.M. Amrei, M. Davoudi, G.G. Chase, H.V. Tafreshi, Effects of roughness on droplet apparent contact angles on a fiber, *Sep. Purif. Technol.* 180 (2017) 107.
- [51] N.M. Farhan, H.V. Tafreshi, Universal expression for droplet–fiber detachment force, *J. Appl. Phys.* 124 (2018), 075301.
- [52] M. Jamali, A. Moghadam, H.V. Tafreshi, B. Pourdeyhi, Droplet adhesion to hydrophobic fibrous surfaces, *Appl. Surf. Sci.* 456 (2018) 626.
- [53] H. Aziz, H.V. Tafreshi, Competing forces on a liquid bridge between parallel and orthogonal dissimilar fibers, *Soft Matter* 15 (35) (2019) 6967–6977.
- [54] M. Jamali, K. Mehta, H. Holweger, M.M. Amrei, H.V. Tafreshi, Controlling detachment residue via magnetic repulsion force, *Appl. Phys. Lett.* 118 (2021), 191601.
- [55] K. Jakhar, A. Chattopadhyay, A. Thakur, R. Raj, Spline based shape prediction and analysis of uniformly rotating sessile and pendant droplets, *Langmuir* 33 (22) (2017) 5603–5612.
- [56] A. Kumar, M.R. Gunjan, K. Jakhar, A. Thakur, R. Raj, Unified framework for mapping shape and stability of pendant drops including the effect of contact angle hysteresis, *Colloids Surf. A Physicochem. Eng. Asp.* 597 (2020), 124619.
- [57] R.E. Johnson, S.S. Sadhal, Fluid mechanics of compound multiphase drops and bubbles, *Annu. Rev. Fluid Mech.* 17 (1985) 289–320.
- [58] S.N. Reznik, A.L. Yarin, E. Zussman, L. Bercovici, Evolution of a compound droplet attached to a core-shell nozzle under the action of a strong electric field, *Phys. Fluids* 18 (2006), 062101.
- [59] J. Guzowski, P.M. Korczyk, S. Jakiela, P. Garstecki, The structure and stability of multiple micro-droplets, *Soft Matter* 8 (2012) 7269.
- [60] F. Weyer, M.B. Said, J. Hotzer, M. Berghoff, L. Dreesen, B. Nestler, N. Vandewalle, Compound droplets on fibers, *Langmuir* 31 (2015) 7799–7805.
- [61] Y. Zhang, D. Chatain, S.L. Anna, S. Garoff, Stability of a compound sessile drop at the axisymmetric configuration, *J. Colloid Interface Sci.* 462 (2016) 88–99.
- [62] S. Bansal, P. Sen, Axisymmetric and nonaxisymmetric oscillations of sessile compound droplets in an open digital microfluidic platform, *Langmuir* 33 (2017) 11047–11058.
- [63] C. Semprenon, G. McHale, H. Kusumaatmaja, Apparent contact angle and contact angle hysteresis on liquid infused surfaces, *Soft Matter* 13 (2017) 101–110.
- [64] N.M. Farhan, H.V. Tafreshi, Using magnetic field to measure detachment force between a nonmagnetic droplet and fibers, *Langmuir* 35 (2019) 8490.
- [65] M. Jamali, H.V. Tafreshi, Measuring force of droplet detachment from hydrophobic surfaces via partial cloaking with ferrofluids, *Langmuir* 36 (2020) 6116.
- [66] H.J. Holweger, M. Jamali, H.V. Tafreshi, Centrifugal detachment of compound droplets from fibers, *Langmuir* 37 (2021) 928.
- [67] A. Marmur, D. Valal, Correlating interfacial tensions with surface tensions: a Gibbsian approach, *Langmuir* 26 (2010) 5568–5575.
- [68] P.K. Roy, B.P. Binks, E. Bormashenko, I. Legchenkova, S. Fujii, S. Shoval, Manufacture and properties of composite liquid marbles, *J. Colloid Interface Sci.* 575 (2020) 35–41.